

Experimental validation of an image-based dynamic pore-network model for spontaneous imbibition in sandstones

Xin Wang ^{a,b}, Chaozhong Qin ^{a,b}, Bo Guo ^c, Sorin Pop ^d, Jian Tian ^{a,b,*}

^a State Key Laboratory of Coal Mine Disaster Dynamics and Control, Chongqing University, Chongqing, China

^b School of Resources and Safety Engineering, Chongqing University, Chongqing, China

^c Department of Hydrology and Atmospheric Sciences, University of Arizona, Tucson, AZ, USA

^d Faculty of Sciences, Hasselt University, Diepenbeek, Belgium

ARTICLE INFO

Keywords:

Spontaneous imbibition
Pore-network modeling
Effective contact angles
Model validation

ABSTRACT

Spontaneous imbibition (SI) in porous media driven by capillary action is pivotal to many subsurface and industrial applications. The pore-scale modeling has been playing a vital role in unraveling wetting dynamics in pore spaces, which will eventually determine flow parameters and behaviors. In this paper, we mainly contribute to validating an image-based dynamic pore-network model (PNM) for SI. For the scenario of water imbibing into dry porous media, we measured imbibition rates and residual saturations of three types of sandstones, namely, Nubian, Bentheimer and Upper Berea as the validation data. Then, we extracted the pore networks of the μ CT images of the same core samples used in the lab experiments, to reduce heterogeneity uncertainties. We demonstrate that using either a uniform or a lognormal distribution of effective contact angles that is consistent with experimental measurements in the literature, the dynamic PNM can accurately predict experimental imbibition rates and residual saturations. Given the challenge of experimentally determining effective contact angles, we further investigate the effects of these two plausible contact angle distributions on the predictions of pore-scale wetting events, relative permeability, capillary pressure, and imbibition rates for more viscous nonwetting fluids. Although uncertainties remain in the preset of effective contact angles, we show that the validated dynamic PNM can provide quantitative and valuable insights into pore-scale wetting dynamics.

1. Introduction

Imbibition is a crucial two-phase flow in porous media where a wetting fluid displaces the defending nonwetting fluid. There exist two distinct imbibition processes, namely, spontaneous imbibition (SI) driven by capillary forces, and forced imbibition induced by a pressure difference across the domain. SI can be further classified into countercurrent and co-current SI. In countercurrent SI, the wetting fluid enters and the nonwetting fluid exits a porous medium via the same boundaries, respectively. In co-current SI, the wetting fluid enters a porous medium through one boundary, while the nonwetting fluid exits the medium through other boundaries. Co-current SI plays pivotal roles in numerous applications such as oil and gas recovery from fracture-rich reservoir (Rangel-German and Kovsek, 2006), paper sensors (Elizalde et al., 2015), and inkjet printing (Wijshoff, 2018). Co-current SI exhibits stronger imbibition dynamics compared to countercurrent SI, making it difficult to predict in pore-scale modeling. Therefore, in this work, we focus on co-current SI in PNM. Unless otherwise specified, SI will refer to as co-current SI throughout the manuscript.

Early studies of co-current SI dynamics on core samples asserted that a frontal advance equation based on the assumption of simultaneous filling of all sizes pores may more accurately depict the true process, compared to a diffusion-like equation that suggests smaller pores fill first (Handy, 1960). In the past decades, analytical scaling of co-current SI experimental data conducted through mass or volume methods has progressed. This has led to the identification of core-scale factors influencing the co-current SI rate, including porosity, intrinsic permeability, pore structure, matrix size, fluid viscosity, initial water saturation, wettability, interfacial tension, capillary pressure, relative permeability, and gravity (Li and Horne, 2004, 2006; Li, 2007). Besides traditional experiments, Zahasky and Benson utilized clinical X-ray computed tomography (CT) to achieve time-lapse visualization of saturation distributions during co-current SI (Zahasky and Benson, 2019). They reported that the roughening of the imbibition front scaled empirically with $t^{-1/4}$, while the imbibition rate was proportional to the square root of imbibition time (Alyafei and Blunt, 2018;

* Corresponding authors.

E-mail addresses: chaozhong.qin@cqu.edu.cn (C. Qin), tianjian2171@cqu.edu.cn (J. Tian).

Shouxiang et al., 1997; Lucas, 1918; Washburn, 1921; Mattax and Kyte, 1962). (Bartels et al., 2019) conducted fast CT scanning combined with the Amott protocol where the flow regime changed from countercurrent to co-current SI. The authors observed that the water-wet samples showed clear SI fronts, while the mixed-wet samples exhibited only localized imbibition sites. With high spatial and temporal resolutions of CT scanning, we can quantify pore-scale fluid displacements. However, previous studies have been predominantly focused on pore-scale events such as Haines jumps (Bultreys et al., 2015; Singh et al., 2017b) and roof snap-off (Andrew et al., 2015; Singh et al., 2019) during drainage, snap-off (Singh et al., 2017a) and ganglion dynamics (Rücker et al., 2015) during flow-rate controlled imbibition, displacement hysteresis during quasi-static drainage and imbibition (Schlüter et al., 2016). With a much higher temporal resolution, microfluidic models allowed for direct observations of pore-scale dynamics of co-current SI (Rangel-German and Kovsek, 2006). Nonetheless, accurately replicating wettability (Zhao et al., 2016) and surface roughness (Buchgraber et al., 2012) of a real rock remains challenging. Due to these limitations in experiments to unravel pore-filling dynamics of co-current SI, the advancement of pore-scale modeling has been necessitated (Blunt et al., 2013; Ramstad et al., 2019).

In general, pore-scale numerical models of co-current SI can be divided into direct numerical simulation (DNS) and dynamic pore-network models (PNM). DNS models are computationally demanding for domains approaching the size of a representative elementary volume (REV). Furthermore, DNS may fail in modeling capillary-dominant two-phase flow such as flow-controlled imbibition with an extremely small capillary number (Shams et al., 2018). DNS models often utilize favorable contact angles due to the deficiency in contact line dynamics. In the image-based modeling, PNM captures the topology and connectivity while approximating the structure as interconnected nodes (i.e., pores) and bonds (i.e., throats) with idealized geometries (Gostick, 2017). Within these pores and throats, simplified physics, such as the relationships among saturation, phase conductance, and capillary pressure, are computed (Joekar-Niasar and Majid Hassanizadeh, 2011; Li et al., 2017; Raeini et al., 2019; Yang et al., 2017; Zhao et al., 2019, 2024). Despite using these simplified geometries and physics, PNM facilitates simulations over much larger domains and with significantly reduced computational effort. By incorporating key flow dynamics through local rules within the pore bodies and throats, PNM can provide valuable insights into pore-scale flow dynamics, and quantitative predictions of intrinsic and relative permeability (Valvatne and Blunt, 2004; Raeini et al., 2019). We note that dynamic two-phase PNM differentiate from each other in the geometries of idealized pore elements (Sun et al., 2016) and critical local rules (Zhao et al., 2024) applied for SI. Recently, Qin and Van Brummelen (2019) developed a μ CT image-based dynamic PNM that accurately represents porous media using properly idealized pore elements. This model implements the competition between main terminal meniscus (MTM) filling and arc menisci (AM) filling (Shouxiang et al., 1997; Patzek and Kristensen, 2001; Patzek and Silin, 2000), which is the most pivotal mechanism in SI. This model has been verified against the volume-of-fluid (VOF) model (one type of DNS) in terms of saturation profiles and imbibition rates under different uniform contact angles and viscosity ratios (wetting to nonwetting viscosities) during co-current SI (Qin et al., 2021). However, the model still lacks experimental validation for realistic rocks, which will be the focus of this paper.

To the best of our knowledge, an accurate representation of the wettability behavior of a rock and the fluids it contains during two-phase flow process is an unresolved question (Blunt et al., 2020). Wettability dictates the sequence of fluid invasion and the resulting fluid distribution in co-current SI within a porous rock. This, in turn, affects key constitutive properties, such as capillary pressure and relative permeability. Contact angles (typically used to characterize wettability) are inherently determined by the intermolecular forces between the surface of the solid and the paired fluid, which is known

as intrinsic contact angle. In addition, contact angles in porous media are often variable, scale-dependent and hysteresis due to local variations in mineralogy, coating and surface roughness (Alhammadi et al., 2017; AlRatrou et al., 2018; Khishvand et al., 2016; Singh et al., 2016). This variability creates a distribution of contact angles with both advancing and receding contact angles. Consequently, the fluid displacement direction actively alters the contact angle, termed the effective contact angle, which is mainly utilized as input for numerical models (Armstrong et al., 2021). Recently, in-situ contact angle measurements based on automated algorithms applied to segmented pore-scale X-ray images have emerged. (Lin et al., 2018, 2019) reported that during steady-state water-flood experiment, the mixed-wet Bentheimer showed a measured mean contact angle of 80° with a standard deviation of 17° , the water-wet Bentheimer had a mean contact angle of 66.4° with a standard deviation of 15.1° . The contact angles of Bentheimer are centered at 60° - 70° after nitrogen or hydrogen injection (drainage), brine injection (imbibition), and waiting 12 h (Zhang et al., 2023). It is found that Bentheimer exhibits average contact angles of 54° after imbibition with H_2 -equilibrated brine and 53° after imbibition with non- H_2 -equilibrated brine, respectively, both with standard deviations of 19° (Jangda et al., 2023). However, these in-situ contact angles are measured at steady state and calculated at the three-phase contact line, where image segmentation poses significant challenges. Consequently, these values carry some uncertainty and may not accurately reflect the advancing contact angles required for co-current SI. Furthermore, for co-current SI, the effective contact angle distribution may be narrower (Mascini et al., 2020). Due to contact angle hysteresis, the actual advancing contact angles for co-current SI are likely to be larger (Morrow, 1970; Blunt et al., 2019). Besides these in-situ contact angle measurements, three alternative definitions of wetting, namely, the thermodynamic contact angle (Blunt et al., 2019), the topology-based contact angle (Garfi et al., 2022), and the fluid surface coverage-based contact angle (Sun et al., 2020) were proposed to address multiphase flow in porous media. However, these three methods have not reached a consensus with each other. In this work, we will utilize experimental data to derive the effective contact angles employed in the dynamic PNM of co-current SI. We will demonstrate that the obtained effective contact angles are consistent with values reported in the previous literature.

The remainder of the paper is structured as follows. In Section 2, we present our lab experiments of water (the wetting fluid)-air (the nonwetting fluid) co-current SI in three types of sandstones. In Section 3, we introduce our dynamic PNM for co-current SI. In Section 4, we firstly verify the pore-network extraction. Then, we define two types of contact angle distribution input for the model by validating experimental data. Finally, under different viscosity ratios, we analyze the impact of these two contact angle distributions on pore-filling dynamics, relative permeability, capillary pressure, and imbibition rate. We end up with the main conclusions in Section 5.

2. Lab experiments of co-current SI

In this work, we use sandstones with permeabilities in the order of 0.1 to $10 \mu\text{m}^2$ as our study porous media mainly for two reasons. Firstly, we want to avoid complex rock wettability which is usually hard to characterize. Secondly, we need to ensure high imaging quality of pore spaces and the REV requirement which are important to the PNM. Pore-scale wetting events in these sandstones can happen in hundreds of milliseconds to a few seconds, so that it is still prohibitive to conduct in-situ imaging of SI dynamics at the pore scale. Therefore, we decided to use core-scale imbibition rates and residual saturations as the validation data. In what follows, we will present the details of the used sandstone samples and lab experiments.

Three types of siliciclastic sandstones, namely, Nubian, Bentheimer and Upper Berea, have been used in this work. They are known as benchmarking samples for digital rock physics and two-phase flow

Table 1

Summary of the basic parameters of the tested cores. Residual saturation (s_r) and porosity values are calculated by the traditional mass balance method.

Core label	Diameter (mm)	Length (mm)	Weight of core^{dry} (g)	Weight of core^{si} (g)	Imbibed water weight (g)	Weight of core^{sat} (g)	Saturated water weight (g)	Porosity	s^w after SI	s_r
NS1	25.2	45.5	45.715	49.367	3.652	50.978	5.263	0.232	0.694	0.306
NS2	25.1	45.1	45.598	49.219	3.621	50.831	5.233	0.235	0.692	0.308
NL1	25.1	81.6	79.397	85.795	6.398	88.637	9.24	0.229	0.692	0.308
NL2	25.2	82.4	79.413	86.116	6.703	89.061	9.648	0.235	0.695	0.305
TL3	24.9	100.2	95.368	102.731	7.363	106.484	11.116	0.228	0.662	0.338
TL4	24.8	100.1	94.847	101.991	7.144	105.645	10.798	0.223	0.662	0.338
TL5	24.9	100.3	95.533	102.863	7.33	106.574	11.041	0.226	0.664	0.336
TS1	24.9	49.8	47.404	51.174	3.77	53.085	5.681	0.234	0.664	0.336
TS2	24.7	49.8	47.049	50.697	3.648	52.55	5.501	0.231	0.663	0.337
TS3	25	50	47.51	51.285	3.775	53.198	5.688	0.232	0.664	0.336
TS4	24.9	49.7	47.169	50.858	3.689	52.731	5.562	0.23	0.663	0.337
TS5	24.9	50	47.199	50.876	3.677	52.743	5.544	0.228	0.663	0.337
US1	24.9	49.7	50.284	53.523	3.239	55.171	4.887	0.202	0.663	0.337
US2	25	49.8	50.338	53.559	3.221	55.175	4.855	0.202	0.663	0.337
US3	24.9	49.6	49.906	53.104	3.198	54.741	4.835	0.2	0.661	0.339
US5	24.9	49.8	50.117	53.336	3.219	54.977	4.86	0.201	0.662	0.338
UL1	24.7	100.1	100.298	106.819	6.521	110.119	9.821	0.205	0.664	0.336
UL2	24.9	100.1	100.453	107.058	6.605	110.416	9.963	0.205	0.663	0.337

parameters such as capillary pressure and relative permeability, due to their well-sorted and relatively homogeneous properties (Yi et al., 2017). The majority of minerals in Nubian sandstones are quartz (85%) with some kaolinite (8%), 5% k-feldspar, and 2% other minerals, trapped within the pore system (Hefny et al., 2020). Bentheimer sandstones are also quartz-rich with little trace of accessory minerals (feldspars, clays, iron oxides and carbonate minerals) (Peksa et al., 2015). Upper Berea sandstones are dominated (> 87%) by quartz, K-feldspar and dolomite, while other constituents are clay minerals (kaolinite, illite or smectite, and chlorite) (Bera et al., 2011; Raeini et al., 2014). For each type of rock, cores with a diameter of 2.5 cm and a total length of 20.0 cm were cut and machined from the same rock mass. These were then sectioned into lengths of 5 cm or 10 cm, except for the Nubian sandstones. Throughout the text, the core types are identified by the abbreviations (i.e., N, T, U for Nubian, Bentheimer, and Upper Berea, respectively), and the lengths are identified by the letters (i.e. L and S for long and short cores respectively). Cores after oven drying to constant weight at 60 °C, after water-air co-current SI, and after vacuum saturation with water for at least 24 h are denoted by core^{dry} , core^{si} , core^{sat} , respectively. The weights of these three states were recorded. Then, core-scale porosity and residual saturation (s_r) can be calculated (Alyafei and Blunt, 2018). Table 1 shows the detailed information of the tested cores. Overall, the variations of core-scale porosity and residual saturation are minor for each type of rock.

Because small digital cores of a few millimeters will be used in the PNM and numerical results will be compared with core-scale experimental data, we need to check if a core is homogenous along the axis direction. To this end, we use the medical CT (SOMATOM Scope 16) scanning in the mode of spiral scan to acquire slice-based information. We place the cores horizontally in the scanner domain, with a tube current of 250 mA and an energy level of radiation of 130 kV. In each slice, porosity and water saturation perpendicular to the length can be respectively calculated by (Alyafei et al., 2016):

$$\epsilon = \frac{CT^{\text{sat}} - CT^{\text{dry}}}{CT^w - CT^a}, \quad s^w = \frac{CT^{\text{si}} - CT^{\text{dry}}}{CT^{\text{sat}} - CT^{\text{dry}}} \quad (1)$$

where CT^{dry} , CT^{si} , CT^{sat} are the averaged CT values for core^{dry} , core^{si} , core^{sat} . The CT values of water and air are 0 and -1000 H respectively. Fig. 1 shows the averaged CT values and the calculated ϵ and s^w along each core axis, which indicate that the used cores are pretty homogeneous. For each type of sandstone, the CT results for different cores are very similar. Therefore, here we only present the CT results of the samples that align with those used in the model validation in Section 4.1.

The core-scale porosity and residual saturations by the CT scanning exhibit good agreement with those obtained by the traditional mass balance method, as evidenced in Table 2. Minor discrepancies (less than 5%) exist between the two methods, which can be attributed to two factors. First, the CT scanning of core^{dry} , core^{si} , core^{sat} was conducted following different preparation processes on different days, which caused varied CT imaging conditions and introduced positional errors (Akin and Kovsek, 2003). Second, water in core^{si} , core^{sat} may evaporate during the preparation for scanning. Therefore, in this work, we used the porosity and residual saturations obtained from the mass balance method as the validation data, while the heterogeneous porosity along the core axis, as well as the constant water saturation behind the wetting front, can still be reliably demonstrated.

We have conducted co-current SI experiments for a water-air system at the ambient condition of room temperature of $21 \pm 1^\circ\text{C}$ and atmospheric pressure. The initial stage of co-current SI can be notably influenced by the imbibition area (Akin et al., 2000). For sandstones with permeabilities in the order of 0.1 to $10 \mu\text{m}^2$, water-air co-current SI advances rapidly, making it difficult to establish a uniform water distribution across the entire cross-section at the inlet. Therefore, we chose the experimental apparatus for vertical core placement, similar to the setup used by (Alyafei and Blunt, 2018), as shown in Fig. 2. The experimental setup primarily consists of an OHAUS PMK423 ZH/E balance mounted on a fixed base with a hole, allowing the core to be vertically suspended from the balance's bottom hook; a water reservoir on an adjustable base enables controlled contact of the water surface with the core's bottom surface; a computer connected to the balance records the mass continuously before the start to the end of spontaneous imbibition with an accuracy of 0.001 g per second. Before the spontaneous imbibition begins, the dry core (core^{dry} , i.e., the core after oven-drying to a constant weight) is suspended under the balance without contacting the water surface. The adjustable base is carefully raised until the water surface touches the core's bottom surface, marking the start of spontaneous imbibition. To prevent additional imbibition from submerged areas and evaporation from the sides, the core is enclosed in a heat-shrink tube, allowing air-filled pores in the dry core to be displaced by water only from the top surface. The mass recorded by the computer is monitored throughout the process. Initially, the mass increases rapidly; when it stabilizes at a nearly constant value, spontaneous imbibition is considered complete, at which point the core is referred to as core^{si} . In Fig. 2, we omit the data prior to the mass transition to the plateau stage. We retain the data where the mass is proportional to the square root of the imbibition time, as this is of primary physical significance and is used to calculate the imbibition rate in Section 4.2. The measured imbibition weights versus imbibition time present good repeatability for each type of rock.

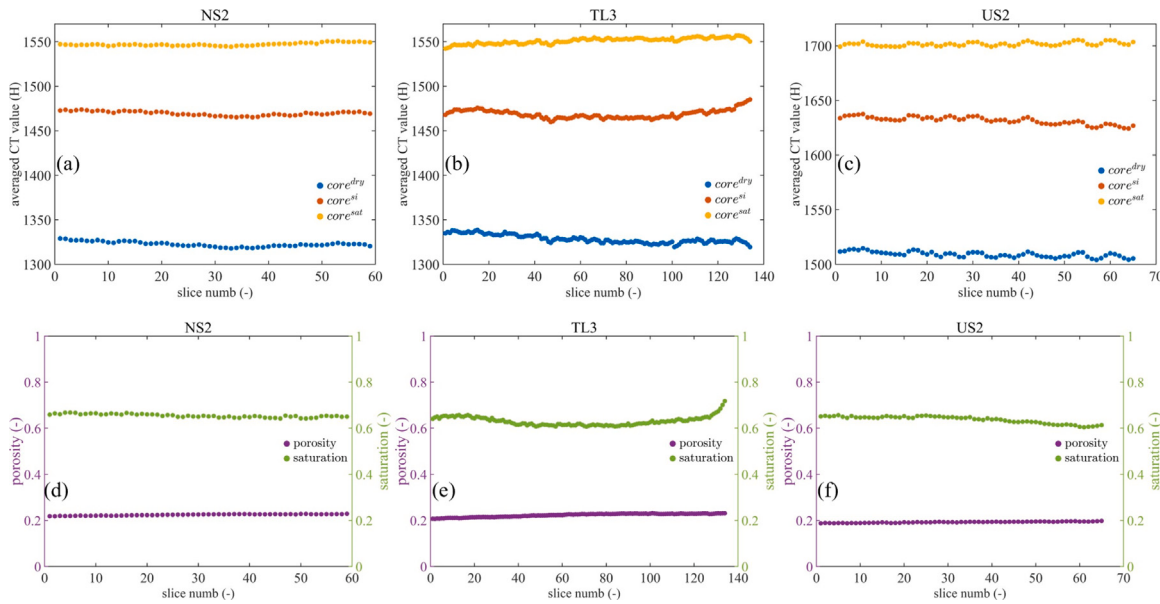


Fig. 1. Averaged CT values for core^{dry} , core^{si} , core^{sat} , and the calculated porosity and water saturations in each CT slice perpendicular to the flow direction of each tested core (TL3, US2, and NS2).

Table 2
Calculated porosity and residual saturations of the three tested cores.

Core label	ϵ calculated by medical CT scanning	s^w calculated by medical CT scanning	s_r calculated by medical CT scanning	ϵ calculated by mass imbibition	s^w calculated by mass imbibition	s_r calculated by mass imbibition
TL3	0.223	0.63	0.37	0.228	0.662	0.338
US2	0.193	0.637	0.363	0.202	0.663	0.337
NS2	0.224	0.654	0.346	0.235	0.692	0.308

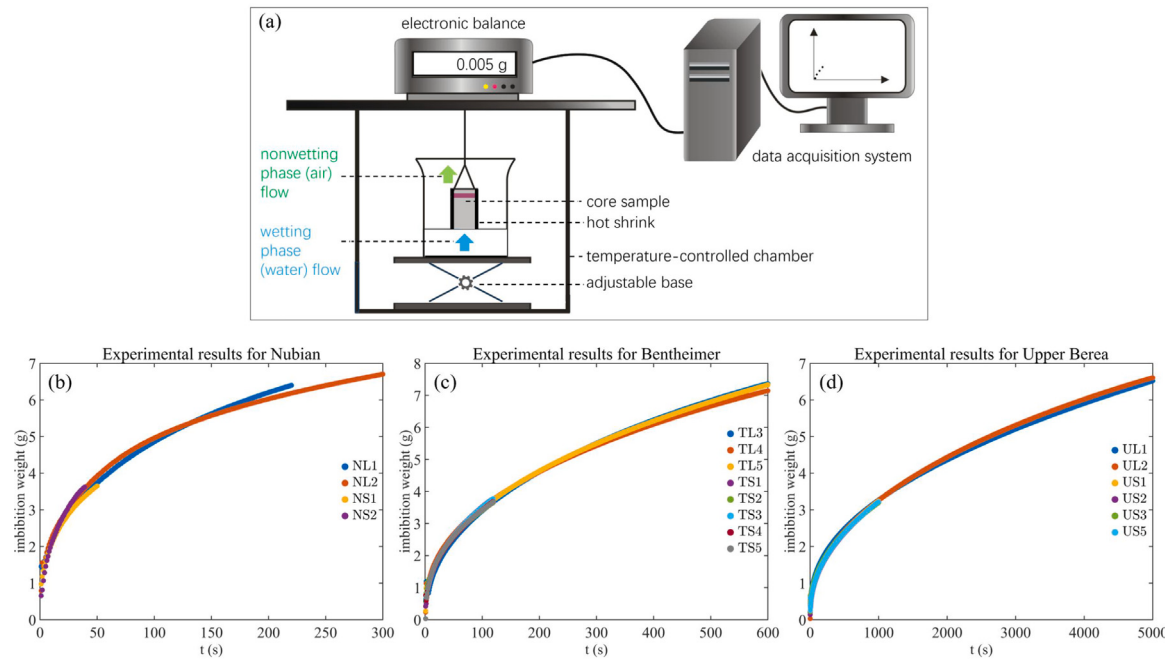


Fig. 2. Schematic of the experimental apparatus for co-current spontaneous imbibition under ambient conditions (a); experimentally measured imbibition curves of imbibed water weights versus imbibition time for Nubian (b), Bentheimer (c) and Upper Berea (d).

3. Dynamic PNM of co-current spontaneous imbibition

In this work, we aim to validate the image-based dynamic PNM of co-current SI presented in (Qin and Van Brummelen, 2019; Qin et al.,

2021). The dynamic model has two distinct features. One is that the model is formulated on multiform pore elements which can properly tackle complex porous structures and a wide range of contact angles. The other is that the model implements the competition between main

terminal meniscus (MTM) filling and arc meniscus (AM) filling, so that it is applicable to a wide range of imbibition processes including co-current SI and forced imbibition. In the following, we briefly present the governing equations and the numerical implementation.

With the assumption of incompressibility, no phase change, and neglecting gravity, the general governing equations for two-phase immiscible flow in a pore network are given by:

$$V_i \frac{ds_i^w}{dt} + \sum_{j=1}^{N_i} K_{ij}^w (p_i^w - p_j^w) = 0 \quad (2a)$$

$$-V_i \frac{ds_i^n}{dt} + \sum_{j=1}^{N_i} K_{ij}^n (p_i^n - p_j^n + p_i^c - p_j^c) = 0 \quad (2b)$$

where the superscripts w and n denote the wetting and nonwetting phases, respectively, N_i is the coordination number of pore body i , representing the number of pores j that are connected to pore i through pore throat ij . In pore body i , V_i is the pore volume, s_i^w is the saturation, K_{ij} is the phase conductivity between the two pore bodies, and capillary pressure (p_i^c) is related to the nonwetting pressure (p_i^n) and wetting pressure (p_i^w) under the assumption of local equilibrium by $p_i^c = p_i^n - p_i^w$. The Eqs. (2a) and (2b) are ordinary different equations and highly nonlinear because both K_{ij} and p^c are functional of the saturation. There have been several numerical schemes for solving the governing equations including the fully implicit scheme (Chen et al., 2020; Wu et al., 2024) and the IMPES (i.e., implicit pressure and explicit saturation) scheme (Thompson, 2002). In the work, we use the IMPES to numerically implement our dynamic PNM of co-current SI (Sheng and Thompson, 2016). Our extensive case studies show that the model preserves good mass balance for both water-air and water-oil systems. For the details of the used local rules and the numerical implementation of the model, one can refer to (Mason and Morrow, 1990; Patzek and Kristensen, 2001; Qin and Van Brummelen, 2019).

The physical parameters utilized in the modeling are detailed in Table 3. A constant surface tension of 0.073 N/m is assumed. Water is used as the wetting phase, with a dynamic viscosity of 1.0×10^{-3} Pa s. The dynamic viscosity of the nonwetting phase is determined by the specified viscosity ratio. At the inlet, we apply a boundary conditions of zero water pressure and a water saturation of unity; to restrict the outflow of the non-wetting phase, we set $K_{ij}^n = 0$ at the inlet pore throat. At the outlet, we impose a boundary condition of zero non-wetting phase pressure and a zero capillary pressure gradient.

4. Results and discussion

Based on the good repeatability among the selected cores shown in Fig. 2, we choose NS2, TL3 and US2 to represent experimental results for Nubian, Bentheimer and Upper Berea sandstones, respectively. To minimize heterogeneity uncertainties, we conduct mercury intrusion porosimetry (MIP) and establish micro-CT image-based pore networks using the remaining sections of the long cores containing NS2, TL3, and US2 to represent each type of sandstone. We use the same pore network for quasi-static drainage and imbibition modeling, as well as dynamic spontaneous imbibition modeling. In this work, the model validation includes both pore-network extraction and numerical predictions of SI rates and residual saturations, which are discussed in Sections 4.1 and 4.2 separately. We will show that in the validation of the PNM for co-current SI, the biggest uncertainty lies in what effective contact angles should be assigned to the model. Therefore, in Section 4.3, we further investigate the impact of two plausible distributions of contact angles on the numerical predictions of wetting events, relative permeability, capillary pressure, and imbibition rates for more viscous nonwetting fluids.

4.1. Image-based extraction of pore networks

The μ CT scanning images of sub-plugs and the images processed by Gaussian blur filter and threshold-based segmentation are shown in Fig. 3. Their geometric information and imaging resolutions are given in Table 3. Nubian and Bentheimer sandstones are both composed of well-characterized, mostly subrounded to rounded grains with sharp edges. Besides, the clear distinction between the gray values of the grains and pores makes pore spaces explicitly discernable. However, for Upper Berea, different mineral phases and rougher mineral edges lead to the difficulty in attributing a certain range of gray values to pore spaces precisely. By visual comparisons of the original and segmented images, sub-resolution microporosity of clays and K-feldspar are segmented as solid under the most appropriate threshold we can apply (Madonna et al., 2012). Notice that the current dynamic PNM does not tackle SI in microporosity. However, the potential impact of neglecting microporosity on our model validation will be considered.

We extracted pore networks by the open-source software PoreSpy with the watershed algorithm (Gostick, 2017). As shown in Fig. 4, the distributions of pore-body sizes for the three digital cores are close to lognormal, with volume-averaged mean values of 12, 23 and 31 μm for Upper Berea, Bentheimer, and Nubian respectively. The coordination number shows a similar distribution, but a smaller mean coordination number for Upper Berea. The other detailed geometric parameters from the PNM are given in Table 3. Compared with the porosity of Upper Berea (0.155), the value by the MIP experiment is 0.208. As mentioned above, this discrepancy is mainly owing to the segmentation of microporosity and minor minerals as solid, which constitute approximately 25% of the total pore volume, as calculated by $(\frac{0.208-0.155}{0.208}) \approx 0.25$. In Bentheimer and Nubian, their proportions are relatively small, at approximately 10% and 3% respectively, using the same calculation method as above.

The PoreSpy provides us with basic geometrical information of pores and their connectivity (i.e. the topology) (Gostick et al., 2019). We then project them into idealized pore elements used in the PNM (Qin et al., 2021). To validate the extraction and the setup of these approximated pore elements, we compare the MIP curve with the Primary Drainage Curve (PDC). For comparison, the MIP curves are scaled down by the ratio of the surface tension between water-air and air-mercury ($\frac{0.073}{0.4865} = 0.15$). Additionally, in the quasi-static primary drainage model, the nonwetting fluid is allowed to invade from all the boundaries rather than the bottom. The contact angle for air-mercury is set to 130° (Saki et al., 2020). As previously mentioned, the Upper Berea, Bentheimer, and Nubian cores contain 25%, 10%, and 3% of their pore volumes in microporosity, respectively. This microporosity cannot be captured in our micro-CT image-based quasi-static PNM. Therefore, we adjust the saturation by: revised saturation = saturation $\times (1 - \phi_m) + \phi_m$, where ϕ_m represents the fraction of microporosity. This adjustment leads to a revised capillary pressure-saturation relationship, referred to as the revised PDC. As seen in Fig. 5, the revised PDC matches the MIP curve better. A slightly higher MIP curve is observed for Nubian, for which the mercury ejection curve is exceptionally absent. This may indicate compaction and collapse of its loose pore structures into smaller pores during mercury intrusion, leading to overestimation of capillary forces and difficulty in mercury withdrawal. Overall, the pore-network extraction for the three types of sandstone can be well justified.

The intrinsic permeability (k^0) is a crucial parameter in the model validation. We need to confirm that the extracted pore networks can accurately predict permeabilities using the PNM. Initially, we intended to experimentally measure the permeabilities of the cores under confining pressures, and then extrapolate the values under the ambient conditions. However, we observe strong hysteresis of permeabilities under confining pressures which indicates profound alterations of pore structures. Given the homogeneity of the used cores, alternatively, we decided to use LBM (Lattice-Boltzmann Model) solver in AVIZO

Table 3

Geometrical and physical parameters used in the case studies.

Parameters	Cores		
	NS2	TL3	US2
μCT data			
Number of voxels in X, Y, and Z directions	900 × 900 × 900		
Voxel resolution (μm)	4	3	2
Pore network information			
Number of pores/pore throats	9913/20455	9091/17863	8750/16955
Numbers of inlet/outlet pores	304/285	256/238	272/263
Volume-averaged mean pore diameter (μm)	31	23	12
Porosity (excluding isolated pores)	0.2056	0.2023	0.1482
Porosity (including isolated pores)	0.2058	0.2031	0.1506
Porosity by MIP	0.2127	0.2271	0.2084
k^0 by the PNM (μm^2)	5.560	2.183	0.209
k^0 by Avizo software (μm^2)	x y z	7.059 6.199 5.868	2.154 2.179 2.143
in X, Y, and Z directions			
within a 600-voxel cubic			
Physical parameters in the modeling			
Surface tension at 21 °C (N/m)	0.073		
Wet (water)/nonwet (air) dynamic viscosity (Pa s)	1.0×10^{-3} / 1.79×10^{-5} (viscosity ratio= 55.9)		
Inlet/outlet reservoir pressure (Pa)	0/0		
Pre-wetting film capillary pressure (Pa)	10^6		

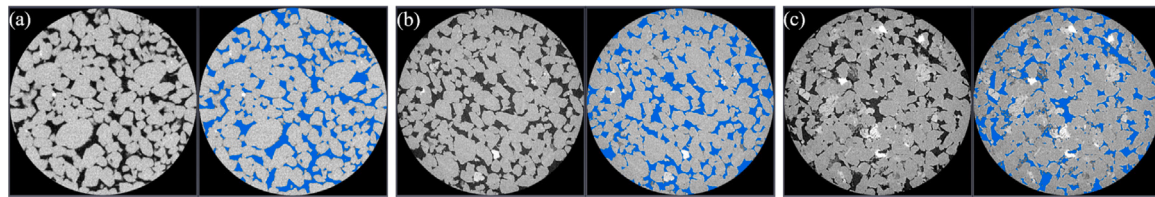


Fig. 3. Raw CT images (left) and CT images processed by Gaussian blur filter and interactive thresholding segmentation (right) from miniplugs of NS2 (a), TL3 (b), and US2 (c) cores.

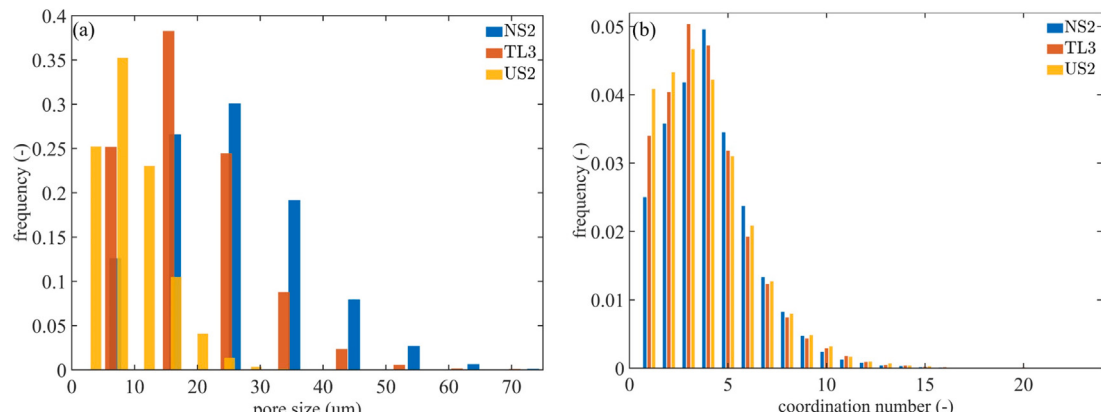


Fig. 4. (a) Distributions of pore size, and (b) distributions of coordination number generated from the pore network for three tested cores.

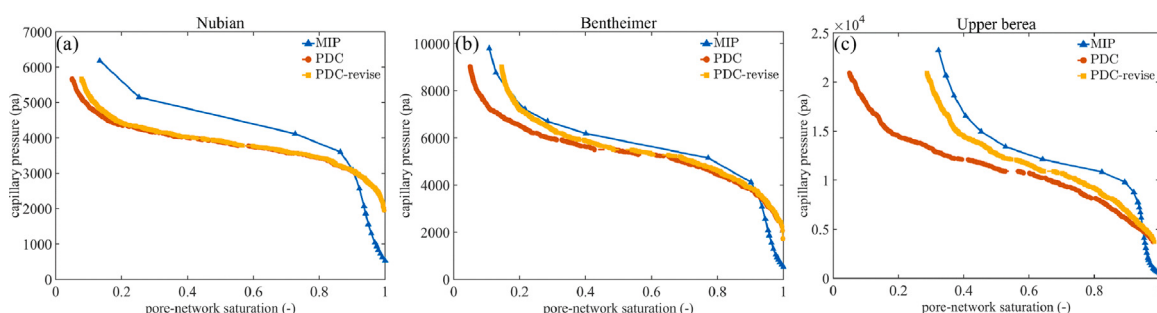


Fig. 5. The comparison between the capillary pressure curves by the MIP (Mercury Intrusion Porosimetry) and by the quasi-static PNM. PDC represents the primary drainage curve. The PDC-revise is obtained by reproducing actual mercury intrusion by adjusting surface tension, contact angle, and invading from surroundings. (a) is for Nubian, (b) is for Bentheimer, and (c) is for Upper Berea.

to verify our PNM for predicting k^0 . We simulated k^0 for a 600³ cubic voxel subvolume extracted from the center of a 900³ cylindrical digital rock. This size was selected due to geometric and computational constraints, and at this scale, k^0 has stabilized, indicating that it reaches REV. As shown in Table 3, k^0 predicted by the PNM match well with the values by the LBM. Finally, it is worth noting that neglected micro-porosity in the digital cores will have a minor impact on the modeling of k^0 because microporosity does not hinder main flow pathways.

To sum up, the complexity of porous structures increases progressively from Nubian to Bentheimer and then to Upper Berea. This information will be referred to in the model validation.

4.2. Validation of the dynamic PNM

The PNM validation against the lab experiments for the water-air system proceeds as follows. To begin with, the experimental data requires post-processing. Because there is a huge distinction between the experimental and numerical lengths, we normalize their penetration length (L [m]) by their medium length (L^0 [m]), $L^* = \frac{L}{L^0}$. Then, we compare the slope values of $\frac{L^*}{\sqrt{t}}$ at each dimensionless penetration length where t [s] is the imbibition time (Qin et al., 2022). The experimental slope is derived by the forward difference. Besides, we check the ratio of capillary force to gravity by inversed Bond number N_B^{-1} , defined as $\frac{C\sigma\sqrt{\epsilon}}{\Delta\rho g L^0}$, where ϵ is porosity, k^0 is intrinsic permeability, $\Delta\rho$ is the difference in density between the two fluid phases (water and air), g is the acceleration due to gravity, and the dimensionless constant C assumes a value of 0.4 for a cylindrical geometry (Schechter et al., 1994). For imbibition processes, $N_B^{-1} > 5$ indicates capillary-dominated flow, whereas $N_B^{-1} \ll 1$ means gravity-dominated flow. The calculated bond numbers are about 12.71, 9.44, 58.75 respectively for Nubian, Bentheimer, and Upper Berea (Schechter et al., 1994; Xu et al., 2019). All values indicate capillary-dominated flow for each sandstone, with smaller values suggesting a greater influence of gravity. We observe slight declines in imbibition slopes along the core length as shown in Fig. 6, which are relatively obvious for Nubian and Bentheimer, as expected due to their relatively smaller Bond numbers.

As a first attempt, we focus on the PNM validation in terms of imbibition rate and residual saturation for Bentheimer (the sample of medium complexity in this work). As shown in Fig. 6b, we observe that the overall trend of experimental imbibition rates can be predicted by the PNM by assuming an advancing contact angle of 75°. On the other hand, previous study indicates that contact angles may follow a lognormal distribution (Jangda et al., 2023); for co-current SI, the effective contact angle distribution is likely narrower (Mascini et al., 2020). Furthermore, quartz-rich sandstones typically exhibit a static contact angle of around 40° (Deng et al., 2018); actual advancing contact angles are generally higher due to contact angle hysteresis (Morrow, 1970; Blunt et al., 2019). Therefore, we establish a range for advancing (or effective) contact angles as a lognormal distribution with a standard deviation of 0.2, constrained between 40° and 90° to ensure water wetting. Then, we adjust the mean value of this distribution until the predicted slope match the experimental results, ultimately yielding a value of 65°. In addition, as shown in Table 4, both predicted residual saturations (i.e., 0.30 under the constant contact angle of 75°, and 0.32 under the lognormal distribution) match the experimental value of 0.34.

Subsequently, we applied the contact angles calibrated by Bentheimer to Nubian and Upper Berea samples in the further PNM validation, considering that they are all siliceous sandstones. For Nubian, the matches of imbibition rates as shown in Fig. 6a and residual saturations given in Table 4 are satisfactory. However, for Upper Berea as shown in Fig. 6c, the predicted imbibition rates are noticeably nearly 50% higher than the experimental data. One contributing factor to the observed discrepancies is the presence of microporosity and minor minerals with exceptionally strong capillary forces. They can rapidly imbibe water (up

to 25% of the total), delaying water uptake in larger pores. This delayed imbibition in larger pores may consequently lead to a reduction in the overall imbibition rate by 25% maximum. On the other hand, effective contact angles do not rely solely on intermolecular interactions between solid and fluids (Behnoudfar et al., 2022). Pinning effects caused by complicated rock surface roughness and the converging/diverging geometry of pore spaces in Upper Berea may cause larger contact angles than those suitable for Nubian and Bentheimer (Herminghaus, 2000; Nosonovsky and Bhushan, 2008). This is the other contributing factor to the observed discrepancies. Nonetheless, the two factors mentioned above barely impact the residual saturation at the end of SI as shown in Table 4.

Finally, it is important to note that we have validated the reproducibility of predictions under lognormally distributed contact angles. We randomly generated five different sets of contact angles, all ranging from 40° to 90° with a standard deviation of 0.2. As illustrated in Fig. A.1 of Appendix A, the comparison results under these five sets of contact angles show a high degree of consistency in predicted imbibition rate, residual saturation, capillary pressure, and relative permeability for Bentheimer, under a viscosity ratio of 55.9.

To sum up, we have shown that the validated dynamic PNM with two plausible distributions of effective contact angles can adequately predict experimental imbibition rates and residual saturations under the water-air system. Both predicted imbibition rates initially increase and then decrease due to the inlet effect, while the use of a single REV size contributes to an overall declining slope that ultimately stabilizes. Furthermore, even within quartz-rich sandstones, those possessing more complex pore structures can lead to higher effective contact angles as inputs in the PNM. Currently, experimental measurements of advancing contact angles during co-current SI remains challenging. Although in-situ contact angle measurements exhibit uncertainty due to the influences of noise in the imaging process, pore structure control and hysteresis, they can provide a potential range for contact angles. For instance, Lin et al. found that during steady-state water-flood experiments, water-wet Bentheimer had a mean contact angle of 66.4° with a standard deviation of 15.1° (Lin et al., 2018), generally agrees with our results. Given that a uniform contact angle has been extensively used in pore-scale modeling for co-current SI, it is worthwhile to investigate the impact of these two plausible distributions of contact angles on numerical predictions.

4.3. Impacts of the distribution of contact angles on numerical predictions

4.3.1. Pore-filling events

Wettability and viscosity ratio together influence the interaction between capillary forces and viscous forces, thereby notably impacting pore-filling events in co-current SI. We note that three sandstones show very similar impacts of the contact angle distribution on numerical predictions. Therefore, in what follows, we will take Bentheimer as an example, unless otherwise stated. The predicted results for Nubian and Upper Berea are shown in Appendix B.

Fig. 7 illustrates wetting phase distribution in each pore at an overall pore network saturation of 0.3, with effective contact angles conforming to both a lognormal distribution and a constant value of 75° (refer to Section 4.2). At a viscosity ratio of 55.9 where the viscous force by the nonwetting phase is negligible and the imbibition dynamic is strong, the co-filling of all-size pores by the wetting phase is observed, leading to a sharp wetting front. As the viscosity ratio decreases, small pores are preferentially filled, which is most pronounced in the quasi-static imbibition. This diminishment of imbibition dynamics broadens the wetting front, and gives rise to a much larger residual saturation, as shown in Table 4. It is found that at the same viscosity ratio, the wetting front under the lognormal distribution of contact angles is discernibly rougher. This can be attributed to two reasons. First, diverse contact angles in the lognormal distribution lead to increased pore-scale heterogeneity of effective pore sizes (i.e., entry pressures), thereby

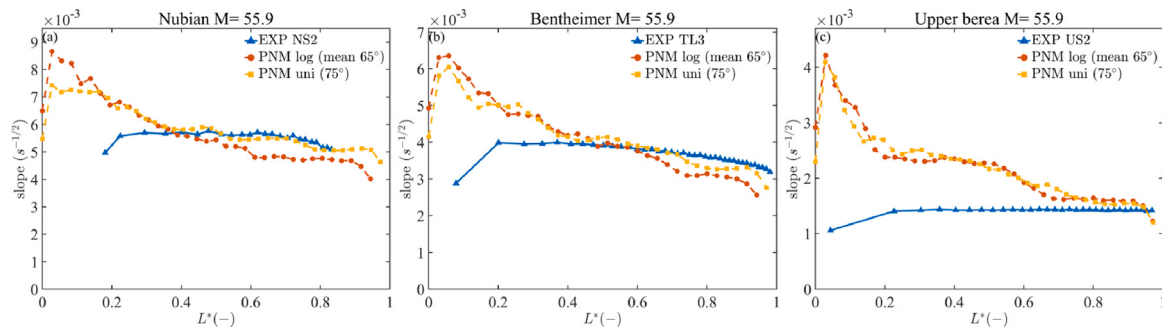


Fig. 6. Imbibition rates obtained from the dynamic PNM and lab experiments for Nubian (a), Bentheimer (b), Upper Berea (c), where the viscosity ratio, $\frac{\mu_{\text{water(water)}}}{\mu_{\text{nonwater(air)}}} = 55.9$.

Table 4

Residual saturations at the end of co-current SI for the tested cores (Nubian, Bentheimer, Upper Berea) from water-air experiments (EXP); dynamic PNM results (Dy) with viscosity ratios of 55.9 ($M = 55.9$), 1 ($M = 1$), 0.1 ($M = 0.1$); quasi-static PNM results (Qs). The model results are based on a uniform contact angle of 75° and a lognormal distribution with a mean value of 65°.

Cores	Contact angle	EXP	Dy ($M = 55.9$)	Dy ($M = 1$)	Dy ($M = 0.1$)	Qs
Nubian	Uni 75°		0.26	0.4	0.52	0.68
	Log 65°	0.31	0.28	0.4	0.48	0.55
Bentheimer	Uni 75°		0.3	0.42	0.52	0.66
	Log 65°	0.34	0.32	0.42	0.5	0.6
Upper Berea	Uni 75°		0.28	0.42	0.54	0.62
	Log 65°	0.34	0.3	0.44	0.52	0.57

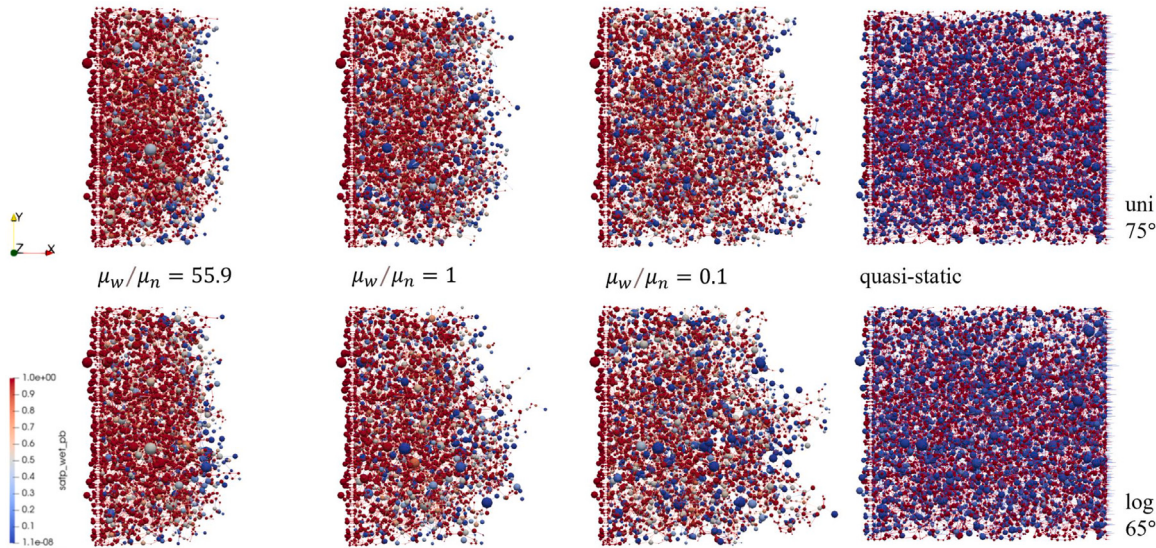


Fig. 7. Wetting distributions when the pore network saturation equals 0.3, under uniform (top row) and lognormal distribution (bottom row) of effective contact angles, with three viscosity ratios of 55.9, 1, 0.1, and quasi-static imbibition (from left to right). For better visualization of saturation in each pore, pores without water are not shown.

causing varied wetting phase distribution in pores. Second, for each pore with a uniform high contact angle of 75°, the wetting phase is geometrically impossible to accumulate in corners. Relatively smaller contact angles in the lognormal distribution promote corner flows in some pores. Especially at a viscosity ratio of 0.1, it is seen that AMs filling and snap-off span a few small pores just at the wetting front.

4.3.2. Relative permeability and average capillary pressure

First, we investigate the effect of contact angle distributions on relative permeability. Fig. 8 shows that for both contact angle distributions, as the viscosity ratio decreases, relative permeability curves become flatter, and shift to the lower left moving closer to the quasi-static ones. This arises from the preferential filling of small pores under a decreased viscosity ratio, trapping the nonwetting phase in some large pores. Subsequently, the fluid flow is impeded, therefore causing lower relative

permeability. Moreover, rougher imbibition fronts may contribute to advantageous conducting pathways, allowing for the breakthrough of the wetting phase at a smaller critical saturation. At the same viscosity ratio, the curves predicted under the lognormal distribution of contact angles become less steep with lower critical saturation and smaller relative permeability at the residual saturation. This phenomenon is attributed to heterogeneous flows under distributed contact angles, which potentially enables the wetting phase to form continuous pathways and breakthrough earlier. This simultaneously induces more entrapment of the nonwetting phase during flow, reducing the relative permeability. Additionally, especially for lower viscosity ratio, slight AMs filling and snap-off observed in the front under contact angle distribution may also create faster but blocked flow.

Then, we focus on the average capillary pressure-saturation curves as shown in Fig. 9. In the quasi-static process, as expected, the curve

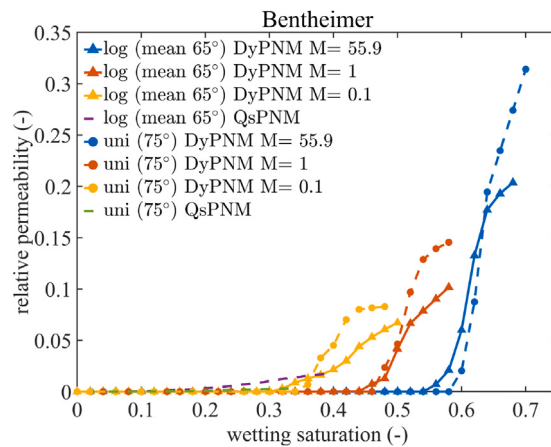


Fig. 8. Wetting relative permeability curves predicted by the quasi-static model and the dynamic PNM with different viscosity ratios under a contact angle of 75° and contact angles with a lognormal distribution.

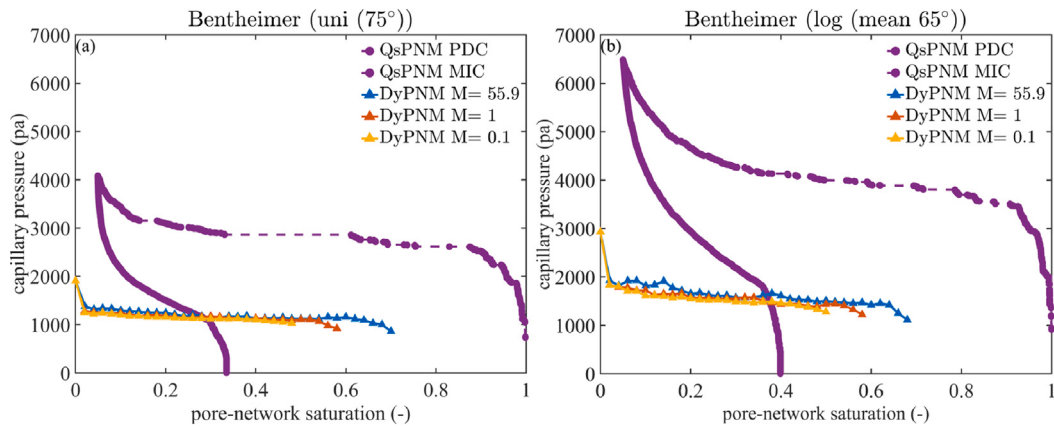


Fig. 9. Capillary pressure curves predicted by the quasi-static PNM and the dynamic PNM with different viscosity ratios (M) under a contact angle of 75° (a) and contact angles with a lognormal distribution (b). The abbreviations of PDC, MIC, and PNM represent the primary drainage curve, the main imbibition curve, and the PNM, respectively.

predicted by contact angles following a lognormal distribution is steeper, compared to that predicted by a constant value. For dynamic spontaneous imbibition, it is observed that the curves remain nearly constant, suggesting pronounced imbibition dynamics. Moreover, as the viscosity ratio decreases, the curve shifts slightly downward. Additionally, under each viscosity ratio, the average capillary pressure predicted by a lognormal distribution with contact angles ranging from 40° to 90° is higher than that predicted by a uniform contact angle of 75°, which is correlated to its higher quasi-static capillary pressure.

4.3.3. Imbibition rates

We compare the imbibition rates under the two distributions of contact angles across varied viscosity ratios. For the water-air system that satisfies the assumption of a sharp wetting front and a constant front saturation, s^f , the analytical solution for the network saturation with respect to the imbibition time is provided by (Qin et al., 2021):

$$s^w = \sqrt{\frac{2k^w p^c s^f}{\varepsilon \mu^w L^2}} \sqrt{t} \quad (3)$$

where k^w is the wetting permeability, p^c is the capillary pressure, ε is the porosity, μ^w is the wetting dynamic viscosity, L is the wetting penetration length. As seen in Fig. 10, at the viscosity ratio of 55.9, the predicted imbibition rates exhibit square root relationships with imbibition time. As confirmed by the experimental validation, imbibition rates under two types of contact angle distributions are comparable. As the decrease of viscosity ratio, we see more and more discrepancy in the imbibition rates between the two contact angle distributions.

Furthermore, it is worth noting that we do not see a straight line (i.e. a linear relationship) at the viscosity ratio of 1.0 and a concave upward line at the viscosity of 0.1, because only REV-size digital rocks are used in the modeling.

Finally, we note that in the case studies presented in this work, spontaneous imbibition is predominantly controlled by the MTM. This phenomenon is observed under specified conditions. First, the contact angles validated by core experiments are relatively large, which geometrically suppresses corner flow. Second, the studied pore network domain size is 900 × 900 × 900, where spontaneous imbibition remains in its early stage. Even with a low viscosity ratio of 0.1, corner flow is founded to be limited to a few pores at the imbibition front for lognormally distributed contact angles ranging from 40° to 90°. In other words, the predicted imbibition rate may exhibit more notable discrepancies under the two types of contact angles when corner flow plays a more substantial role in spontaneous imbibition. This can occur when the study domain is very long and the imbibition is at its late stage.

5. Conclusion

In this work, we have established comprehensive experimental data of co-current spontaneous imbibition (SI) in three types of sandstones, namely, Nubian, Bentheimer, and Upper Berea. The scenario of water imbibed into a dry porous rock was considered. To reduce uncertainties, the μ CT images of the mini plugs from the same cores in the experiments were used to extract the pore networks. We have

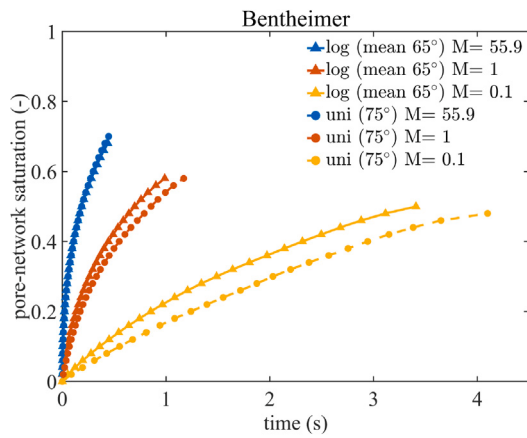


Fig. 10. Overall saturation versus the imbibition time predicted by the dynamic PNM with different viscosity ratios under a contact angle of 75° and contact angles with a lognormal distribution.

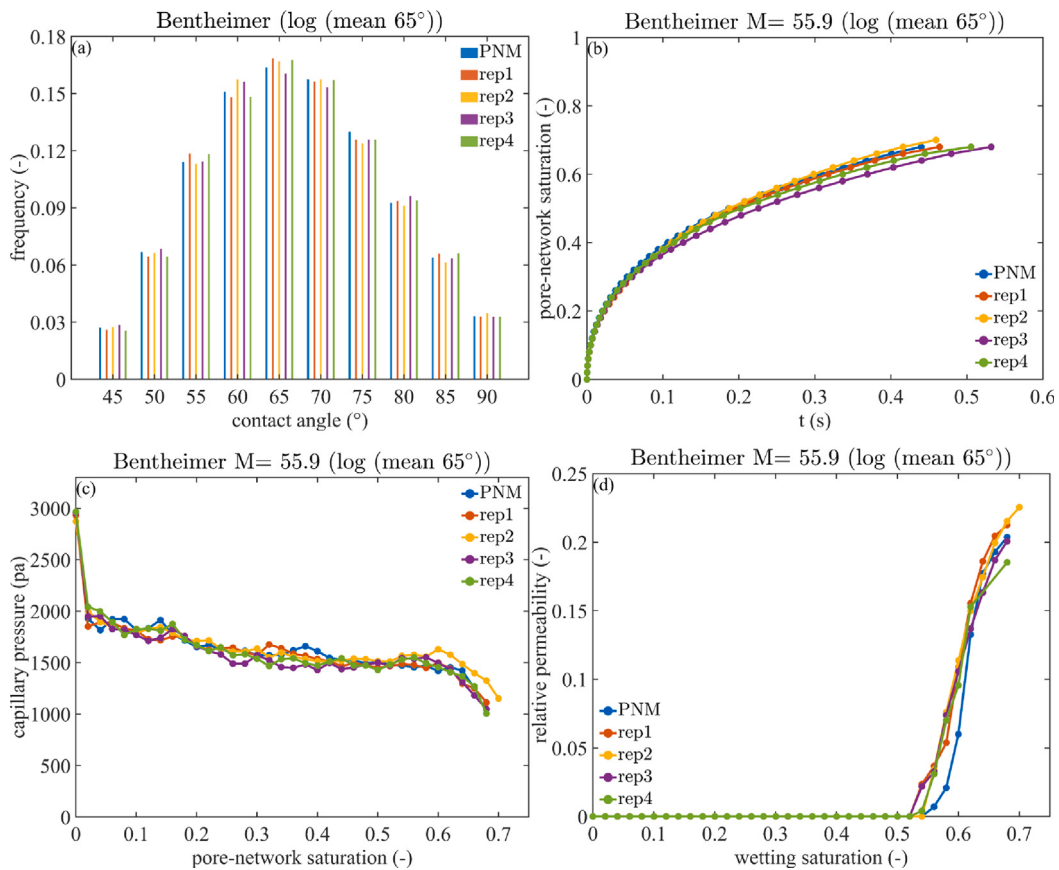


Fig. A.1. (a) Five kinds of contact angle distributions in the same form (lognormal distribution ranging from 40° to 90° with a standard deviation of 0.2). (b) Predicted imbibition rate, (c) relative permeability and (d) capillary pressure across these distributions, under the water-air system for Bentheimer.

validated an image-based dynamic PNM in terms of imbibition rate and residual saturation. Based on our validation and case studies, the main conclusions are drawn as follows:

1. For Nubian and Bentheimer, with either uniform (75°) or a lognormal distribution (from 40° to 90° with a mean value of 65°) of effective contact angles, the dynamic PNM can adequately predict water-air experimental imbibition rates and residual saturations. The derived lognormal distribution agrees well with previous studies.

2. In the context of co-current SI, Upper Berea sandstones exhibit higher effective contact angles compared to Nubian and Bentheimer, attributed to the more complex porous structures of Upper Berea in terms of pore morphology and coordination number.

3. With a lognormal distribution of effective contact angles, the dynamic PNM predicts rougher wetting fronts, slightly faster imbibition rates at low viscosity ratios, significantly higher capillary pressures, and lower relative permeability.

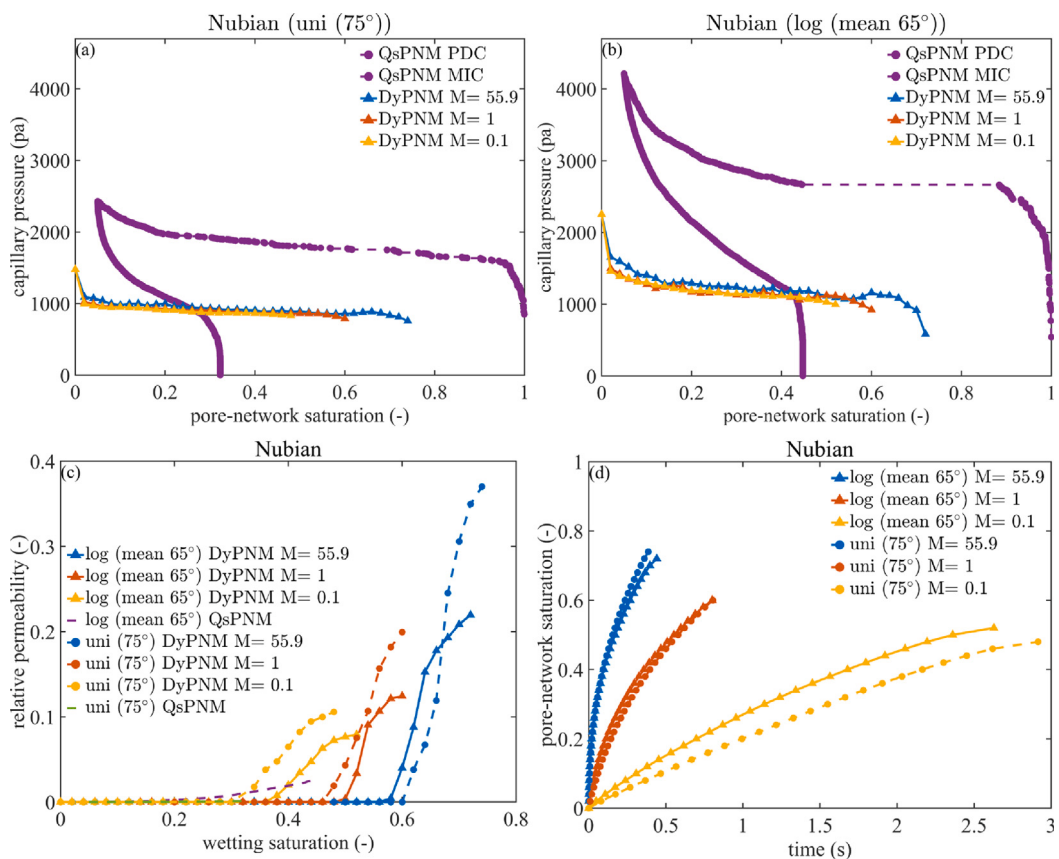


Fig. B.1. Predicted results for Nubian. Capillary pressure curves predicted by the quasi-static PNM and the dynamic PNM with different viscosity ratios under a contact angle of 75° (a) and contact angles with a lognormal distribution (b). Wetting relative permeability curves predicted by the quasi-static PNM and the dynamic PNM with different viscosity ratios under a contact angle of 75° and contact angles with a lognormal distribution (c). Overall saturation versus the imbibition time predicted by the dynamic PNM with different viscosity ratios under a contact angle of 75° and contact angles with a lognormal distribution (d).

CRediT authorship contribution statement

Xin Wang: Writing – original draft, Visualization, Validation, Software, Resources, Investigation, Formal analysis, Data curation. **Chaozhong Qin:** Writing – review & editing, Supervision, Project administration, Methodology, Funding acquisition, Conceptualization. **Bo Guo:** Writing – review & editing, Supervision, Resources. **Sorin Pop:** Writing – review & editing, Resources, Investigation. **Jian Tian:** Writing – review & editing, Formal analysis.

Declaration of competing interest

The authors declare that they have no known competing financial interests or personal relationships that could have appeared to influence the work reported in this paper.

Acknowledgments

C.Z.Q. acknowledges the support of National Natural Science Foundation of China (No. 12072053, No. 12211530480). S.P. acknowledges the support of FWO-NSFC project VS03823N.

Supplementary materials

The dataset associated with the present work is available via <https://doi.org/10.6084/m9.figshare.26869819.v2>.

Appendix A. The repeatability test of lognormal-distributed contact angles

We generate 5 kinds of contact angle distributions in the same form (lognormal distribution ranging from 40° to 90° with a standard deviation of 0.2) as shown in Fig. A.1. We compare predicted results under the water-air system for Bentheimer to evaluate repeatability. The predictions in Fig. A.1 indicate that imbibition rate, relative permeability and capillary pressure remain consistent across these distributions. This uniformity suggests that different contact angle distributions of the same form do not significantly impact these key parameters. So in the main text, the first kind of contact angle distribution and its predictions are detailed.

Appendix B. The predicted results for Nubian and upper Berea

Predicted trends in Nubian (Fig. B.1) and Upper Berea (Fig. B.2) are the same as those in Bentheimer. The variability in contact angles across pores leads to enhanced fluctuations and upper bounds in $P^C - S$ curve. At the same viscosity ratio, relative permeability-saturation curves predicted under the lognormal distribution of contact angles become flatter with lower critical saturation and reduced relative permeability at the residual saturation. As the viscosity ratio decreases, curves become flatter and shift to the lower left, moving closer to quasi-static parts. Both contact angle distributions that are validated for the water-air system, manifest variations in imbibition rates and wetting saturation when extended to other viscosity ratios.

The distinction among these three cores lies in that for Upper Berea, the predicted results under the two types of contact angles

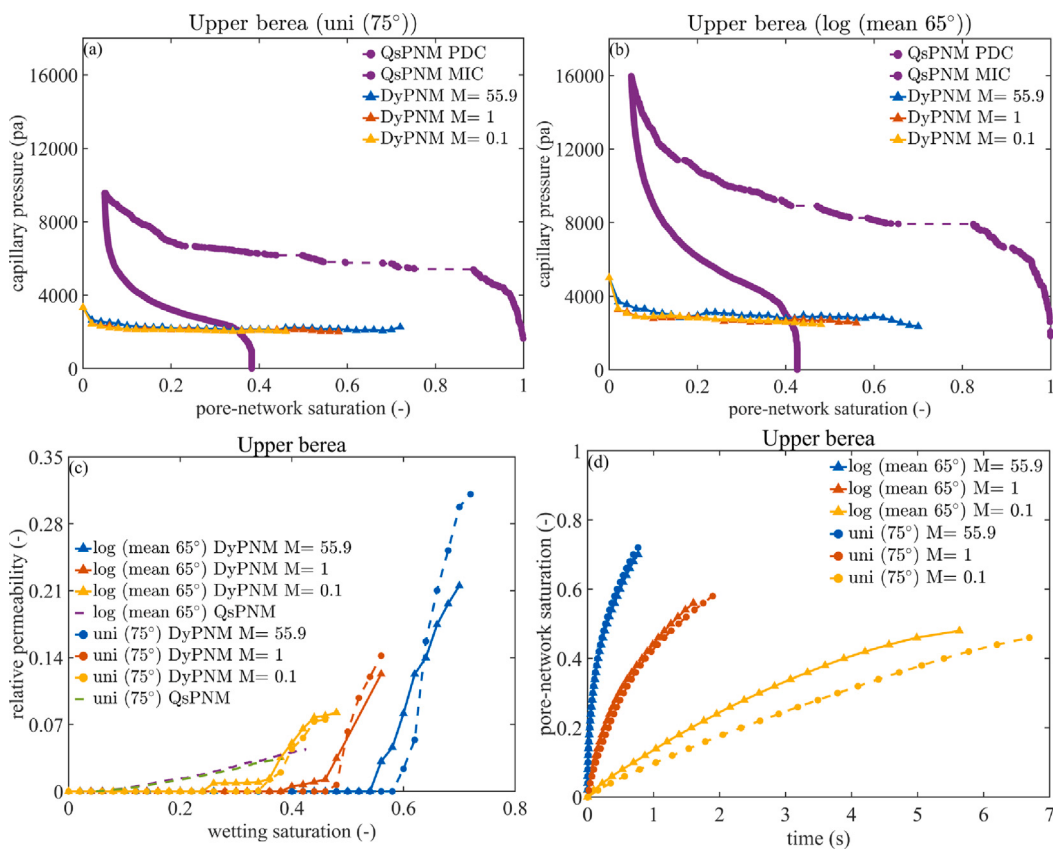


Fig. B.2. Predicted results for Upper Berea. Capillary pressure curves predicted by the quasi-static PNM and the dynamic PNM with different viscosity ratios under a contact angle of 75° (a) and contact angles with a lognormal distribution (b). Wetting relative permeability curves predicted by the quasi-static PNM and the dynamic PNM with different viscosity ratios under a contact angle of 75° and contact angles with a lognormal distribution (c). Overall saturation versus the imbibition time predicted by the dynamic PNM with different viscosity ratios under a contact angle of 75° and contact angles with a lognormal distribution (d).

exhibit greater discrepancies, more prominently manifested in capillary pressure and imbibition rate. This is because cores with inherently complex pore structures exhibit greater sensitivity to the distribution of contact angles, and additionally, a larger REV is required for modeling, particularly for flow parameters.

Data availability

Data will be made available on request.

References

- Akin, S., Kovscek, A.R., 2003. Computed tomography in petroleum engineering research. *Geol. Soc. London Special Publ.* 215 (1), 23–38. <http://dx.doi.org/10.1144/GSL.SP.2003.215.01.03>.
- Akin, S., Schember, J.M., Bhat, S.K., Kovscek, A.R., 2000. Spontaneous imbibition characteristics of diatomite. *J. Pet. Sci. Eng.* 25, 149–165. [http://dx.doi.org/10.1016/S0920-4105\(00\)00010-3](http://dx.doi.org/10.1016/S0920-4105(00)00010-3).
- Alhammad, A.M., AlRatrou, A., Singh, K., Bijeljic, B., Blunt, M.J., 2017. In situ characterization of mixed-wettability in a reservoir rock at subsurface conditions. *Sci. Rep.* 7, 10753. <http://dx.doi.org/10.1038/s41598-017-10992-w>.
- AlRatrou, A., Blunt, M.J., Bijeljic, B., 2018. Wettability in complex porous materials, the mixed-wet state, and its relationship to surface roughness. *Proc. Natl. Acad. Sci.* 115, 8901–8906. <http://dx.doi.org/10.1073/pnas.1803734115>.
- Alyafei, N., Al-Menhal, A., Blunt, M.J., 2016. Experimental and analytical investigation of spontaneous imbibition in water-wet carbonates. *Transp. Porous Media* 115, 189–207. <http://dx.doi.org/10.1007/s11242-016-0761-4>.
- Alyafei, N., Blunt, M.J., 2018. Estimation of relative permeability and capillary pressure from mass imbibition experiments. *Adv. Water Resour.* 115, 88–94. <http://dx.doi.org/10.1016/j.advwatres.2018.03.003>.
- Andrew, M., Menke, H., Blunt, M.J., Bijeljic, B., 2015. The imaging of dynamic multiphase fluid flow using synchrotron-based X-ray microtomography at reservoir conditions. *Transp. Porous Media* 110, 1–24. <http://dx.doi.org/10.1007/s11242-015-0553-2>.
- Armstrong, R.T., Sun, C., Mostaghimi, P., Berg, S., Rücker, M., Luckham, P., Georgiadis, A., McClure, J.E., 2021. Multiscale characterization of wettability in porous media. *Transp. Porous Media* 140, 215–240. <http://dx.doi.org/10.1007/s11242-021-01615-0>.
- Bartels, W.-B.R.M., Boone, M., Bultreys, T., Mahani, H., Berg, S., Hassanzadeh, S.M., Cnudde, V., 2019. Imaging spontaneous imbibition in full Darcy-scale samples at pore-scale resolution by fast X-ray tomography. *Water Resour. Res.* 55, 7072–7085. <http://dx.doi.org/10.1029/2018WR024541>.
- Behnoudfar, D., Dragila, M., Meisenheimer, D., Wildenschild, D., 2022. Contact angle hysteresis: A new paradigm? *Adv. Water Resour.* 161, 104138. <http://dx.doi.org/10.1016/j.advwatres.2022.104138>.
- Bera, B., Mitra, S.K., Vick, D., 2011. Understanding the micro structure of Berea sandstone by the simultaneous use of micro-computed tomography (micro-CT) and focused ion beam-scanning electron microscopy (FIB-SEM). *Micron* 42, 412–418. <http://dx.doi.org/10.1016/j.micron.2010.12.002>.
- Blunt, M.J., Akai, T., Bijeljic, B., 2020. Evaluation of methods using topology and integral geometry to assess wettability. *J. Colloid Interface Sci.* 576, 99–108. <http://dx.doi.org/10.1016/j.jcis.2020.04.118>.
- Blunt, M.J., Bijeljic, B., Dong, H., Gharbi, O., Iglauer, S., Mostaghimi, P., Paluszny, A., Pentland, C., 2013. Pore-scale imaging and modelling. *Adv. Water Resour.* 51, 197–216. <http://dx.doi.org/10.1016/j.advwatres.2012.03.003>.
- Blunt, M.J., Lin, Q., Akai, T., Bijeljic, B., 2019. A thermodynamically consistent characterization of wettability in porous media using high-resolution imaging. *J. Colloid Interface Sci.* 552, 59–65. <http://dx.doi.org/10.1016/j.jcis.2019.05.026>.
- Buchgraber, M., Kovscek, A.R., Castanier, L.M., 2012. A study of microscale gas trapping using etched silicon micromodels. *Transp. Porous Media* 95, 647–668. <http://dx.doi.org/10.1007/s11242-012-0067-0>.
- Bultreys, T., Boone, M.A., Boone, M.N., De Schryver, T., Masschaele, B., Van Loo, D., Van Hoorebeke, L., Cnudde, V., 2015. Real-time visualization of Haines jumps in sandstone with laboratory-based microcomputed tomography. *Water Resour. Res.* 51, 8668–8676. <http://dx.doi.org/10.1002/2015WR017502>.
- Chen, S., Qin, C., Guo, B., 2020. Fully implicit dynamic pore-network modeling of two-phase flow and phase change in porous media. *Water Resour. Res.* 56, <http://dx.doi.org/10.1029/2020WR028510>, e2020WR028510.
- Deng, Y., Xu, L., Lu, H., Wang, H., Shi, Y., 2018. Direct measurement of the contact angle of water droplet on quartz in a reservoir rock with atomic force microscopy. *Chem. Eng. Sci.* 177, 445–454. <http://dx.doi.org/10.1016/j.ces.2017.12.002>.

- Elizalde, E., Urteaga, R., Berli, C.L.A., 2015. Rational design of capillary-driven flows for paper-based microfluidics. *Lab Chip* 15 (10), 2173–2180. <http://dx.doi.org/10.1039/C4LC01487A>.
- Garf, G., John, C.M., Rücker, M., Lin, Q., Spurin, C., Berg, S., Krevor, S., 2022. Determination of the spatial distribution of wetting in the pore networks of rocks. *J. Colloid Interface Sci.* 613, 786–795. <http://dx.doi.org/10.1016/j.jcis.2021.12.183>.
- Gostick, J.T., 2017. Versatile and efficient pore network extraction method using marker-based watershed segmentation. *Phys. Rev. E* 96, 023307. <http://dx.doi.org/10.1103/PhysRevE.96.023307>.
- Gostick, J., Khan, Z., Tranter, T., Kok, M., Agnaou, M., Sadeghi, M., Jervis, R., 2019. PoreSpy: A Python toolkit for quantitative analysis of porous media images. *J. Open Source Softw.* 4, 1296. <http://dx.doi.org/10.21105/joss.01296>.
- Handy, L.L., 1960. Determination of effective capillary pressures for porous media from imbibition data. *Trans. AIME* 219, 75–80. <http://dx.doi.org/10.2118/1361-G>.
- Hefny, M., Qin, C., Saar, M.O., Ebibgo, A., 2020. Synchrotron-based pore-network modeling of two-phase flow in Nubian sandstone and implications for capillary trapping of carbon dioxide. *Int. J. Greenh. Gas Control* 103, 103164. <http://dx.doi.org/10.1016/j.ijggc.2020.103164>.
- Herminghaus, S., 2000. Roughness-induced non-wetting. *Europhys. Lett.* 52, 165. <http://dx.doi.org/10.1209/epl/i2000-00418-8>.
- Jangda, Z., Menke, H., Busch, A., Geiger, S., Bultreys, T., Lewis, H., Singh, K., 2023. Pore-scale visualization of hydrogen storage in a sandstone at subsurface pressure and temperature conditions: Trapping, dissolution and wettability. *J. Colloid Interface Sci.* 629, 316–325. <http://dx.doi.org/10.1016/j.jcis.2022.09.082>.
- Joekar-Niasar, V., Majid Hassanzadeh, S., 2011. Effect of fluids properties on non-equilibrium capillarity effects: Dynamic pore-network modeling. *Int. J. Multiph. Flow* 37, 198–214. <http://dx.doi.org/10.1016/j.ijmultiphaseflow.2010.09.007>.
- Khishvand, M., Alizadeh, A.H., Piri, M., 2016. In-situ characterization of wettability and pore-scale displacements during two- and three-phase flow in natural porous media. *Adv. Water Resour.* 97, 279–298. <http://dx.doi.org/10.1016/j.advwatres.2016.10.009>.
- Li, K., 2007. Scaling of spontaneous imbibition data with wettability included. *J. Contam. Hydrol.* 89, 218–230. <http://dx.doi.org/10.1016/j.jconhyd.2006.09.009>.
- Li, K., Horne, R.N., 2004. An analytical scaling method for spontaneous imbibition in gas/water/rock systems. *SPE J.* 9, 322–329. <http://dx.doi.org/10.2118/88996-PA>.
- Li, K., Horne, R.N., 2006. Generalized scaling approach for spontaneous imbibition: An analytical model. *SPE reserv. Eval. Eng.* 9, 251–258. <http://dx.doi.org/10.2118/77544-PA>.
- Li, J., McDougall, S.R., Sorbie, K.S., 2017. Dynamic pore-scale network model (PNM) of water imbibition in porous media. *Adv. Water Resour.* 107, 191–211. <http://dx.doi.org/10.1016/j.advwatres.2017.06.017>.
- Lin, Q., Bijeljic, B., Berg, S., Pini, R., Blunt, M.J., Krevor, S., 2019. Minimal surfaces in porous media: Pore-scale imaging of multiphase flow in an altered-wettability Bentheimer sandstone. *Phys. Rev. E* 99, 063105. <http://dx.doi.org/10.1103/PhysRevE.99.063105>.
- Lin, Q., Bijeljic, B., Pini, R., Blunt, M.J., Krevor, S., 2018. Imaging and measurement of pore-scale interfacial curvature to determine capillary pressure simultaneously with relative permeability. *Water Resour. Res.* 54, 7046–7060. <http://dx.doi.org/10.1029/2018WR023214>.
- Lucas, R., 1918. Über das Zeitgesetz des kapillaren Aufstiegs von Flüssigkeiten. *Kolloid-Zeitschrift* 23, 15–22. <http://dx.doi.org/10.1007/BF01461107>.
- Madonna, C., Almqvist, B.S., Saenger, E.H., 2012. Digital rock physics: numerical prediction of pressure-dependent ultrasonic velocities using micro-CT imaging: Digital rock physics. *Geophys. J. Int.* 189 (3), 1475–1482. <http://dx.doi.org/10.1111/j.1365-246X.2012.05437.x>.
- Mascini, A., Cnudde, V., Bultreys, T., 2020. Event-based contact angle measurements inside porous media using time-resolved micro-computed tomography. *J. Colloid Interface Sci.* 572, 354–363. <http://dx.doi.org/10.1016/j.jcis.2020.03.099>.
- Mason, G., Morrow, N.R., 1990. Capillary behavior of a perfectly wetting liquid in irregular triangular tubes. *J. Colloid Interface Sci.* 141, [http://dx.doi.org/10.1016/0021-9797\(91\)90321-X](http://dx.doi.org/10.1016/0021-9797(91)90321-X).
- Mattax, C., Kyte, J., 1962. Imbibition oil recovery from fractured, water-drive reservoir. *Soc. Pet. Eng. J.* 2 (02), 177–184. <http://dx.doi.org/10.2118/187-PA>.
- Morrow, N.R., 1970. Physics and thermodynamics of capillary action in porous media. *Ind. Eng. Chem.* 62, 32–56. <http://dx.doi.org/10.1021/ie50726a006>.
- Nosonovsky, M., Bhushan, B., 2008. Roughness-induced superhydrophobicity: a way to design non-adhesive surfaces. *J. Phys.: Condens. Matter.* 20, 225009. <http://dx.doi.org/10.1088/0953-8984/20/22/225009>.
- Patzek, T.W., Kristensen, J.G., 2001. Shape factor correlations of hydraulic conductance in noncircular capillaries. *J. Colloid Interface Sci.* 236, 305–317. <http://dx.doi.org/10.1006/jcis.2000.7414>.
- Patzek, T.W., Silin, D.B., 2000. Shape Factor and Hydraulic Conductance in Noncircular Capillaries: I. One-Phase Creeping Flow, <http://dx.doi.org/10.1006/jcis.2000.7413>.
- Peksa, A.E., Wolf, K.-H.A.A., Zitha, P.L.J., 2015. Bentheimer sandstone revisited for experimental purposes. *Mar. Pet. Geol.* 67, 701–719. <http://dx.doi.org/10.1016/j.marpetgeo.2015.06.001>.
- Qin, C.-Z., Van Brummelen, H., 2019. A dynamic pore-network model for spontaneous imbibition in porous media. *Adv. Water Resour.* 133, 103420. <http://dx.doi.org/10.1016/j.advwatres.2019.103420>.
- Qin, C.-Z., Van Brummelen, H., Hefny, M., Zhao, J., 2021. Image-based modeling of spontaneous imbibition in porous media by a dynamic pore network model. *Adv. Water Resour.* 152, 103932. <http://dx.doi.org/10.1016/j.advwatres.2021.103932>.
- Qin, C.-Z., Wang, X., Zhang, H., Hefny, M., Jiang, H., Tian, J., Deng, W., 2022. Numerical studies of spontaneous imbibition in porous media. *J. Pet. Sci. Eng.* 218, 110961. <http://dx.doi.org/10.1016/j.petrol.2022.110961>.
- Raeini, A.Q., Blunt, M.J., Bijeljic, B., 2014. Direct simulations of two-phase flow on micro-CT images of porous media and upscaling of pore-scale forces. *Adv. Water Resour.* 74, 116–126. <http://dx.doi.org/10.1016/j.advwatres.2014.08.012>.
- Raeini, A.Q., Yang, J., Bondino, I., Bultreys, T., Blunt, M.J., Bijeljic, B., 2019. Validating the generalized pore network model using micro-CT images of two-phase flow. *Transp. Porous Media* 130, 405–424. <http://dx.doi.org/10.1007/s11242-019-01317-8>.
- Ramstad, T., Berg, C.F., Thompson, K., 2019. Pore-scale simulations of single- and two-phase flow in porous media: Approaches and applications. *Transp. Porous Media* 130, 77–104. <http://dx.doi.org/10.1007/s11242-019-01289-9>.
- Rangel-German, E.R., Kovsek, A.R., 2006. A micromodel investigation of two-phase matrix-fracture transfer mechanisms. *Water Resour. Res.* 42 (2004WR), 003918. <http://dx.doi.org/10.1029/2004WR003918>.
- Rücker, M., Berg, S., Armstrong, R.T., Georgiadis, A., Ott, H., Schwing, A., Neiteler, R., Brussee, N., Makurata, A., Leu, L., Wolf, M., Khan, F., Enzmann, F., Kersten, M., 2015. From connected pathway flow to Ganglion dynamics. *Geophys. Res. Lett.* 42, 3888–3894. <http://dx.doi.org/10.1002/2015GL064007>.
- Saki, M., Siahpoush, S., Khaz'ali, A.R., 2020. A new generalized equation for estimation of sandstone and carbonate permeability from mercury intrusion porosimetry data. *J. Pet. Explor. Prod. Technol.* 10, 2637–2644. <http://dx.doi.org/10.1007/s13202-020-00900-w>.
- Schechter, D.S., Zhou, D., Orr, F.M., 1994. Low IFT drainage and imbibition. *J. Pet. Sci. Eng.* 11, 283–300. [http://dx.doi.org/10.1016/0920-4105\(94\)90047-7](http://dx.doi.org/10.1016/0920-4105(94)90047-7).
- Schlüter, S., Berg, S., Rücker, M., Armstrong, R.T., Vogel, H.-J.H.R., Wildenschild, D., 2016. Pore-scale displacement mechanisms as a source of hysteresis for two-phase flow in porous media. *Water Resour. Res.* 52, 2194–2205. <http://dx.doi.org/10.1002/2015WR018254>.
- Shams, M., Raeini, A.Q., Blunt, M.J., Bijeljic, B., 2018. A numerical model of two-phase flow at the micro-scale using the volume-of-fluid method. *J. Comput. Phys.* 357, 159–182. <http://dx.doi.org/10.1016/j.jcp.2017.12.027>.
- Sheng, Q., Thompson, K., 2016. A unified pore-network algorithm for dynamic two-phase flow. *Adv. Water Resour.* 95, 92–108. <http://dx.doi.org/10.1016/j.advwatres.2015.12.010>.
- Shouxiang, M., Morrow, N.R., Zhang, X., 1997. Generalized scaling of spontaneous imbibition data for strongly water-wet systems. *J. Pet. Sci. Eng.* 18 (3), 165–178. [http://dx.doi.org/10.1016/S0920-4105\(97\)00020-X](http://dx.doi.org/10.1016/S0920-4105(97)00020-X).
- Singh, K., Bijeljic, B., Blunt, M.J., 2016. Imaging of oil layers, curvature and contact angle in a mixed-wet and a water-wet carbonate rock. *Water Resour. Res.* 52, 1716–1728. <http://dx.doi.org/10.1002/2015WR018072>.
- Singh, K., Jung, M., Brinkmann, M., Seemann, R., 2019. Capillary-dominated fluid displacement in porous media. *Annu. Rev. Fluid Mech.* 51, 429–449. <http://dx.doi.org/10.1146/annurev-fluid-010518-040342>.
- Singh, K., Menke, H., Andrew, M., Lin, Q., Rau, C., Blunt, M.J., Bijeljic, B., 2017a. Dynamics of snap-off and pore-filling events during two-phase fluid flow in permeable media. *Sci. Rep.* 7, 5192. <http://dx.doi.org/10.1038/s41598-017-05204-4>.
- Singh, K., Scholl, H., Brinkmann, M., Michiel, M.D., Scheel, M., Herminghaus, S., Seemann, R., 2017b. The role of local instabilities in fluid invasion into permeable media. *Sci. Rep.* 7, 444. <http://dx.doi.org/10.1038/s41598-017-00191-y>.
- Sun, Y., Karaghani, A., Tsotsas, E., 2016. Micro-model experiments and pore network simulations of liquid imbibition in porous media. *Chem. Eng. Sci.* 150, 41–53. <http://dx.doi.org/10.1016/j.ces.2016.04.055>.
- Sun, C., McClure, J.E., Mostaghimi, P., Herring, A.L., Berg, S., Armstrong, R.T., 2020. Probing effective wetting in subsurface systems. *Geophys. Res. Lett.* 47, e2019GL086151, <http://dx.doi.org/10.1029/2019GL086151>.
- Thompson, K.E., 2002. Pore-scale modeling of fluid transport in disordered fibrous materials. *AIChE J.* 48, 1369–1389. <http://dx.doi.org/10.1002/aic.690480703>.
- Valvatne, P.H., Blunt, M.J., 2004. Predictive pore-scale modeling of two-phase flow in mixed wet media. *Water Resour. Res.* 40 (7), <http://dx.doi.org/10.1029/2003WR002627>.
- Washburn, E.W., 1921. The dynamics of capillary flow. *Phys. Rev.* 17, 273–283. <http://dx.doi.org/10.1103/PHYSREV.17.273>.
- Wijshoff, H., 2018. Drop dynamics in the inkjet printing process. *Curr. Opin. Colloid Interface Sci.* 36, 20–27. <http://dx.doi.org/10.1016/j.cocis.2017.11.004>.
- Wu, H., Veyskarami, M., Schneider, M., Helmig, R., 2024. A new fully implicit two-phase pore-network model by utilizing regularization strategies. *Transp. Porous Media* 151, 1–26. <http://dx.doi.org/10.1007/s11242-023-02031-2>.
- Xu, D., Bai, B., Wu, H., Hou, J., Meng, Z., Sun, R., Li, Z., Lu, Y., Kang, W., 2019. Mechanisms of imbibition enhanced oil recovery in low permeability reservoirs: Effect of IFT reduction and wettability alteration. *Fuel* 244, 110–119. <http://dx.doi.org/10.1016/j.fuel.2019.01.118>.
- Yang, J., Bondino, I., Regaieg, M., Moncorgé, A., 2017. Pore to pore validation of pore network modelling against micromodel experiment results. *Comput. Geosci.* 21, 849–862. <http://dx.doi.org/10.1007/s10596-017-9630-7>.

- Yi, Z., Lin, M., Jiang, W., Zhang, Z., Li, H., Gao, J., 2017. Pore network extraction from pore space images of various porous media systems. *Water Resour. Res.* 53, 3424–3445. <http://dx.doi.org/10.1002/2016WR019272>.
- Zahasky, C., Benson, S.M., 2019. Spatial and temporal quantification of spontaneous imbibition. *Geophys. Res. Lett.* 46, 11972–11982. <http://dx.doi.org/10.1029/2019GL084532>.
- Zhang, Y., Bijeljic, B., Gao, Y., Goodarzi, S., Foroughi, S., Blunt, M.J., 2023. Pore-scale observations of hydrogen trapping and migration in porous rock: Demonstrating the effect of Ostwald ripening. *Geophys. Res. Lett.* 50, e2022GL102383, <http://dx.doi.org/10.1029/2022GL102383>.
- Zhao, B., MacMinn, C.W., Juanes, R., 2016. Wettability control on multiphase flow in patterned microfluidics. *Proc. Natl. Acad. Sci.* 113, 10251–10256. <http://dx.doi.org/10.1073/pnas.1603387113>.
- Zhao, B., MacMinn, C.W., Primkulov, B.K., Chen, Y., Valocchi, A.J., Zhao, J., Kang, Q., Bruning, K., McClure, J.E., Miller, C.T., Fakhari, A., Bolster, D., Hiller, T., Brinkmann, M., Cueto-Felgueroso, L., Cogswell, D.A., Verma, R., Prodanović, M., Maes, J., Geiger, S., Vassvik, M., Hansen, A., Segre, E., Holtzman, R., Yang, Z., Yuan, C., Chareyre, B., Juanes, R., 2019. Comprehensive comparison of pore-scale models for multiphase flow in porous media. *Proc. Natl. Acad. Sci.* 116, 13799–13806. <http://dx.doi.org/10.1073/pnas.1901619116>.
- Zhao, J., Zhang, G., Wu, K., Qin, F., Fei, L., Derome, D., Carmeliet, J., 2024. Dynamic pore network modeling of imbibition in real porous media with corner film flow. *Langmuir* 40, 7364–7374. <http://dx.doi.org/10.1021/acs.langmuir.3c03534>.